ISSN 0018-1439, High Energy Chemistry, 2024, Vol. 58, No. 5, pp. 527–535. © Pleiades Publishing, Ltd., 2024.

PHOTOCATALYSIS

Investigation of the Electronic Structure of Metal-Doped TiO_2 Photocatalysts

Serap Kırcı[a] (ORCID: 0009-0002-2694-1581), E. Esra Kasapbaşı[b, *] (ORCID: 0000-0002-5854-3580), and Arzu Hatipoglu[a] (ORCID: 0000-0001-9691-3485)

[a] *Yildiz Technical University, Chemistry Department, İstanbul, Turkey*

[b] *Haliç University, Faculty of Arts and Sciences, Department of Molecular Biology and Genetics, İstanbul, Turkey*

**e-mail: esrakasapbasi@halic.edu.tr*

Received April 4, 2024; revised April 4, 2024; accepted May 29, 2024

Abstract—Water contamination is one of the most critical environmental issues, necessitating the development of effective wastewater treatment methods. The utilization of TiO_2 photocatalysts for pollutant removal in wastewater has gained significant attention. This study aims to explore the photocatalytic properties of TiO_2 modified through the introduction of different metal dopants, thus altering its electronic structure. Using the density functional theory (DFT) method, we examined the photocatalytic properties of TiO_2 clusters doped with metals carrying charges of +3, +4, and +5. Our findings indicate that the incorporation of these metals led to reduced energy and increased stability for the majority of TiO_2 clusters. The calculated UV-vis absorption results revealed that the wavelengths of Model B were extended further in the metal cation-doped TiO_2 clusters compared to Model A. Our DFT calculations demonstrated that the photocatalytic activity of the TiO_2 structure was enhanced upon doping with metals of +3, +4, and +5 valence.

Keywords: TiO_2, DFT, molecular modeling, photocatalytic activity, transition metals

DOI: 10.1134/S0018143924700498

INTRODUCTION

The world's most valuable and important natural resource, water, is at risk of contamination by organic pollutants. As the world population increases, the need for water resources is also increasing. Discharge of organic pollutants or toxic substances that are harmful to the environment and cannot be eliminated naturally is the most important cause of water pollution. Therefore, effective methods are needed to remove toxic compounds from water [1–5]. After the discovery of the photocatalytic activity of titanium dioxide (TiO_2) by Honda and Fujishima in 1972, TiO_2 photocatalysis has been used as an advanced oxidation method, especially for the removal of pollutants from wastewater [6, 7].

Thus, various experimental and theoretical studies have been carried out to remove organic pollutants in water by TiO_2 photocatalysis [8–20]. The first step in photocatalysis is to form electron-hole (e^-/h^+) pairs by excitation with light with an energy equal to or higher than the band gap of TiO_2. In the presence of oxygen, these pairs migrate to the interface to give oxidizing species. In liquid suspension systems, electrons are trapped in the cavities (Ti^{3+}) on the surface and react with the adsorbed O_2 to form a superoxide anion radical. The cavities react with surface OH^- groups or water molecules to produce OH radicals. In this way, they can reduce various organic compounds. In order to increase the activity of TiO_2 under visible light, doping with metals, doping with nonmetals, and surface modifications are made [21–23]. There are different photocatalysts such as WO_3, ZnO, ZnS, Fe_2O_3, CdS, and $SrTiO_3$. However, when compared to the stated photocatalysts, TiO_2 is a preferred heterogeneous photocatalyst because it is inexpensive, non-toxic, chemically inert, and photo-stable. TiO_2 has a wide band-gap (~3.2 eV) and it is also ineffective by visible light and can only be excited by UV light. Therefore, most of the work done in recent years has focused on extending the optical absorption of TiO_2 into the visible region of the spectrum by utilizing UV light. For this, various impurities are added to the TiO_2 matrix to reduce the band gap [15]. To modify TiO_2, studies have been carried out with impurities such as metal ion doping, non-metal ion doping, surface modification, and rare earth metals doping. There are many studies in the literature on metal additives, and it has been reported that in most of these studies metal-doped TiO_2 narrows the band gap and increases the photocatalytic activity [24–32]. Also, doping TiO_2 with various non-metals such as C, N, S and N, S co-doping or C, N, S tri-doping is becoming more popular and thus the synergistic effect increases [24, 33–35].

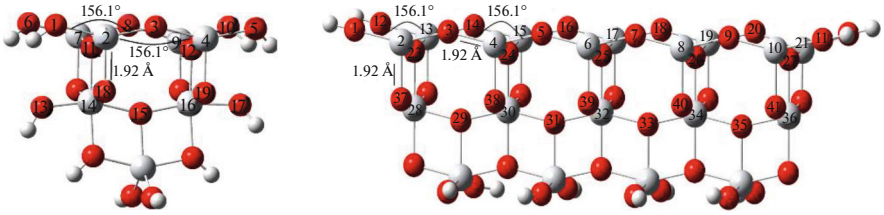

Model A Model B

Fig. 1. Optimized structures of Model A, and Model B by DFT method.

In this study, the design and electronic properties of visible light-sensitive new cation-doped nano TiO_2 photocatalysts were investigated by quantum chemical methods. It is aimed to help the designed photocatalyst models to be used in water purification by utilizing the energy source from the sun. It is explained how cations affect electronic properties in TiO_2 crystal structure. Experimental UV-vis spectra were compared with theoretical UV-vis spectra, and their relationship with electronic structure was explained.

CALCULATION METHOD

In order to determine the effects of different metals on the structural and electronic properties of TiO_2, quantum chemical modeling calculations of TiO_2 and metal-doped TiO_2 were performed. All the calculations were carried out with the DFT method within the Gaussian-16 package [36]. The DFT calculations performed by the hybrid B3LYP functional [37], which combines Hartree–Fock and Becke exchange terms with the Lee–Yang–Parr correlation functional at 6-31G(d) level [38, 39]. Frequency analysis, calculated at the same level of theory, indicates that the optimized structures are at the stationary points corresponding to local minima without any imaginary frequency. UV-vis absorption spectra of the doped and undoped clusters with the lowest energy were calculated by Time-dependent DFT (TD-DFT) method [40]. The 20 lowest energy excited states are calculated. By determining the lowest energy unoccupied orbitals, wavelengths and intensities of possible electronic transitions are obtained. Theoretical UV-vis spectra were obtained with a bandwidth of 200–800 nm at each UV-vis absorbance frequency by fitting a Gaussian curve.

The most widely used crystal form of TiO_2 in heterogeneous photocatalysis is anatase. The surface of the anatase form consists of (1 0 1), (1 0 0), and (0 0 1) crystal planes. In this study, the surface with the highest photocatalytic activity (0 0 1) was modeled with neutral, stoichiometric, finite clusters [41]. The use of neutral clusters in calculations eliminates the problem of giving a specific electrical charge to the cluster. In order to reduce the surface area, the unsaturated titanium atoms on the surface of the models are saturated with hydroxyl and the oxygen atoms with hydrogen. For the anatase model, the experimental parameters of the crystal were used. The unit cell of anatase is tetragonal and its network constants are $a = b = 3.78$ Å and $c = 9.51$ Å [15]. The modeled unit cell, TiO_6, has a slightly distorted octahedral structure with oxygens located at the corners. Each octahedral has eight neighbors. Four of them jointly use an edge, and the other four jointly use a corner. Ti^{4+} cations are bound to six O^{2-} anions and oxygens to three titanium atoms. Doped models, were prepared by replacing the Ti^{4+} ions on the surface of the clusters with metal cations.

Two separate cluster models have been developed for the anatase structure. In models, atoms are systematically numbered. Model A is modeled as the unit cell of anatase with the formula $Ti_7O_{19}H_{10}$ with 36 atoms and is given in Fig. 1. In order to examine the effect of metal doping in larger structures, Model B was developed by repeating Model A along the 4 × 1 × 1 mesh axes. Model B with the formula $Ti_{19}O_{44}H_{12}$ with 75 atoms is given in Fig. 1. Thus, all free valences on the surface are saturated, so that the coordination of Ti atoms is brought to the same number as the atoms in the crystal. Metal-doped models are also modeled by replacing the Ti^{4+} ions on the surface of the clusters with metal cations. While the metal contribution rate is 14.28% in Model A, this rate decreases to 5.26% in Model B. The main reason for working on two different models is to observe the effect of metal doped at different rates on the structure. While calculating the optimum geometric structures of the models, metal ion, H, and OH groups were relaxed by keeping the cluster geometry frozen.

RESULTS AND DISCUSSION

Electronic Structures

The electronic energy levels and band gap energies of the undoped and +3, +4, and +5 value transition metal ions doped TiO_2 clusters of models A and B were calculated. For the developed clusters, the valence band (VB) corresponds to the energy of the highest occupied molecular orbital (E_{HOMO}) and the conduction band (CB) corresponds to the energy of the lowest unoccupied molecular orbitals (E_{LUMO}). By examining

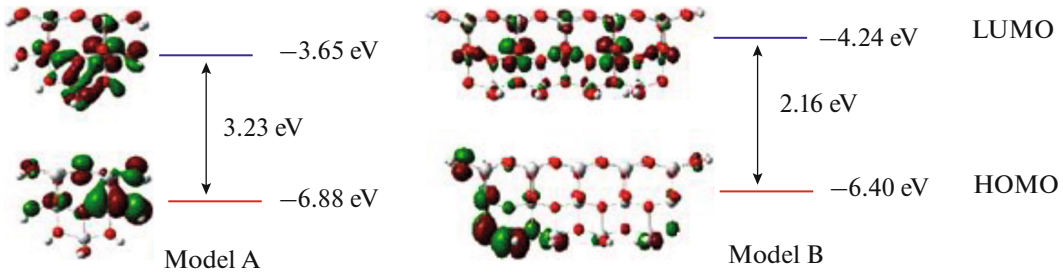

Fig. 2. Frontier molecular orbitals and energies of undoped TiO_2 models.

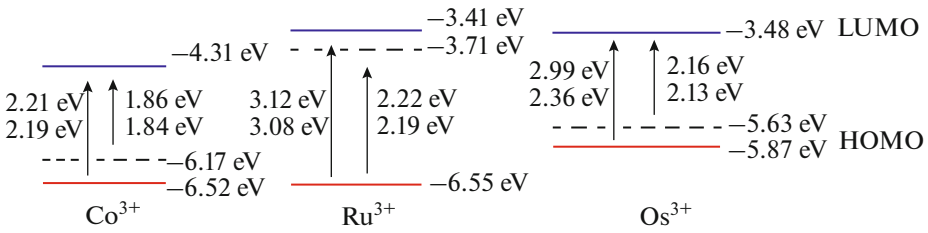

Fig. 3. Electronic energy levels of Model A with +3 metal cation doped.

the band gap diagrams of the transitions in these frontier orbitals, it was determined at which wavelengths the TiO_2 models are active.

Undoped Models

The electronic energy levels of undoped anatase models A and B are shown in Fig. 2 with their frontier orbitals.

It can be seen in Fig. 2 that in undoped TiO_2, the high energy levels of the valence band are filled with 2*p* orbitals of oxygen, while the low energy levels of the conduction band contain the 3d orbitals of titanium. The ΔE value obtained for Model A is very close to the experimental band gap energy of anatase and was calculated as 3.23 eV. For Model B, this value was calculated as 2.16 eV. The experimental band gap energy of the anatase (0 0 1) surface is 3.2 eV, and the band gap energy values found as a result of the calculations are corrected by taking this value as a reference. The calculated band gap values were corrected with the scissor operator. The scissors operator shifts the band gap energy of the occupied and vacant orbitals to the same value as the experimental band gap energy of anatase by shifting the minimum value of the band gap. With the scissor operator, the minimum band gap of the HOMO and LUMO orbitals is shifted to the same value as the experimental band gap of anatase. The wavelengths corresponding to the band gap energies for the undoped models were found to be 383 nm for Model A and 574 nm for Model B.

Tri-Valent Cations Doped Models

The electronic energy levels of the +3 doped clusters are given in Fig. 3 for model A in Fig. SI-1 for model B. Frontier molecular orbital diagrams of +3 doped clusters (Model A and B) are given in supplementary materials. The calculated wavelengths corresponding to the electronic energy levels for all cations doped are given in Table 1 for all doping cations.

Table 1. Band gap energies (eV) and wavelengths (nm) of metal-doped models calculated by the DFT method

Metal	ΔE	λ_{max}	ΔE	λ_{max}
	Model A		Model B	
Ru^{3+}	2.19	566	1.95	635
Os^{3+}	2.13	582	2.75	450
Co^{3+}	1.84	674	3.67	337
Zr^{4+}	3.31	374	3.30	375
Sn^{4+}	2.36	525	2.68	462
Pd^{4+}	1.51	821	1.00	1239
Cr^{4+}	2.34	529	2.32	534
Ge^{4+}	1.96	632	1.97	629
Nb^{5+}	1.22	1016	1.56	794
Sb^{5+}	2.4	516	2.62	473
Ta^{5+}	1.50	826	1.94	639
V^{5+}	0.94	1318	1.42	873

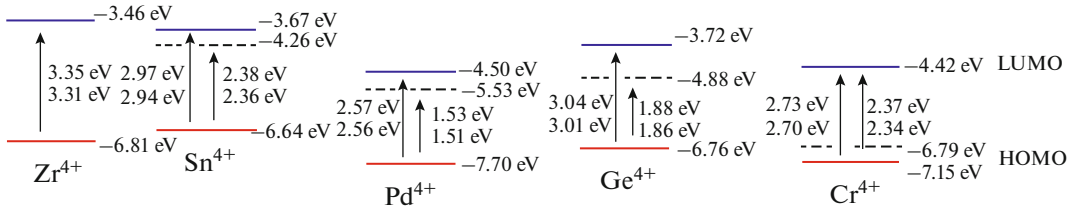

Fig. 4. Electronic energy levels of Model A with +4 metal cation doped.

The additional energy levels in the +3 valent metal doping usually occur from the d orbitals of the metals and they have divided the band gap into two distinct parts. Thus, by absorbing very low-energy photons, electrons can pass from the valence band to the additional half-filled energy levels and then also the conduction band. Additional energy levels contributed to the valence band in Models A and B, resulting in a reduction of the band gap.

Additional energy levels of Co^{3+} are the d orbitals. These additional levels divide the band gap into two parts. Thus, very low-energy photons can be absorbed, and electrons can pass from the valence band to this half-filled additional energy level and pass from there to the conduction band. The additional energy levels for the Ru^{3+} cation are close to the conduction band. So, Ru^{3+} will be an electron scavenger (*n*-type) in photocatalytic reactions. On the other hand, Os^{3+} is also a space-retaining (p-type) in photocatalytic reactions since the additional energy levels are close to the valence band. It was observed that all +3 doped metals increased the photocatalytic activity of TiO_2. The wavelength has increased by about 224 nm. The highest increase was in the Co^{3+} cation with 291 nm, and the least increase was Ru^{3+} with 183 nm.

Tetra-valent Cations Doped Models

The electronic energy levels of the +4 doped clusters are given in Fig. 4, for Model A in Fig. SI-2 for Model B. The frontier molecular orbital diagrams of 4+ clusters (Model A and B) are given in supplementary materials.

In the Sn^{4+} doped models, it is observed that the d orbitals of Sn^{4+} form additional energy levels close to the conduction band. It has been determined that Sn^{4+} does not have a great contribution to the optical and photocatalytic activity of TiO_2, but increases the activity by reducing the band gap by 0.85 eV compared to the undoped TiO_2. Since the energy values are close to the conduction band, Sn^{4+} can increase the photocatalytic activity of TiO_2 by playing an electron-scavenging (*n*-type) role in photocatalytic reactions.

As can be seen, in Fig. 4 the Pd^{4+} cation contributed to the conduction band of TiO_2, causing the band gap to decrease. Thus, light absorption shifts to the visible region when TiO_2 is doped with Pd^{4+}. Additional energy levels in the band gap are the d orbitals of Pd^{4+}, which divide the band gap into two parts. By absorbing low-energy photons, electrons can pass from the valence band to the conduction band with additional energy levels. As seen in Fig. 4, the energies of the additional energy levels in Model A are close to the conduction band, indicating that Pd^{4+} will play a role as an electron-scavenging (*n*-type) in photocatalytic reactions. Conversely, in Model B, the additional band is closer to the valence band.

The Ge^{4+} cation contributed to the conduction band of TiO_2, causing the band gap to decrease. This contribution is slightly higher for Model B than Model A. There are additional energy levels of Ge^{4+} in the band gap. For these levels, the contribution of the d orbitals of Ge^{4+} is the highest as seen in Table 1. The fact that the levels are close to the conduction band indicates that Ge^{4+} will play a role as an electron scavenger in photocatalytic reactions. It shows that doping TiO_2 with Ge^{4+} shifts the light absorption to the visible region by extending it by 249 nm.

Cr^{4+} cation reduced the band gap by contributing to the valence band of TiO_2 in Model A, and the conduction band in Models B. This result shows that doping with Cr^{4+} shifts the light absorption of TiO_2 to the visible region. The d orbitals of Cr^{4+} contribute the most to the additional energy levels in the band gap and also increase the photocatalytic activity of TiO_2. It was observed that Zr-doped Model A did not contribute to the valence band and conduction band, while Model B contributed slightly to the conduction band. This may be due to the diameter of the Zr^{4+} ion being larger than the Ti^{4+} ion. Compared to the undoped model Zr has moved away from the model surface in the doped models.

Penta-valent Cations Doped Models

The electronic energy levels of the +5 doped clusters are given in Fig. 5 for Model A, and in Fig. SI-3 for Model B. The frontier molecular orbitals of +5 clusters (Model A and B) are given in supplementary materials. The wavelengths obtained from these energy values are also given in the Table 1. The band gap energy was significantly 2 eV reduced in the Nb^{5+}

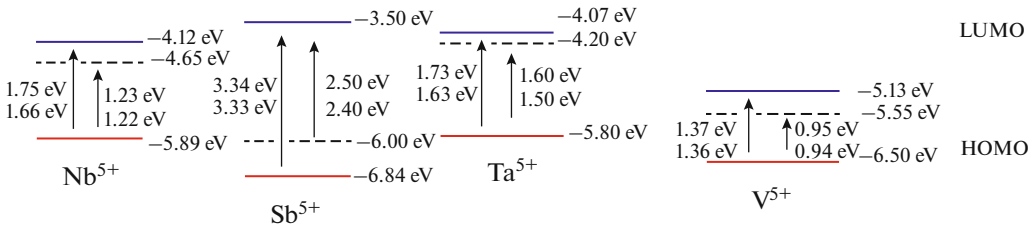

Fig. 5. Electronic energy levels of Model A with +5 metal cation doped.

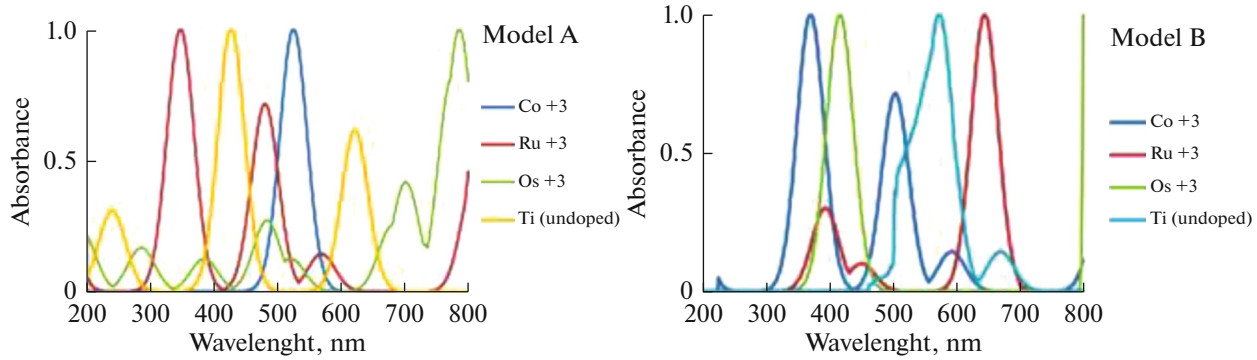

Fig. 6. Calculated UV-vis spectra of doped 3+ cations.

cation doped models. The d orbitals of Nb^{5+} cations contributed significantly to the conduction band of the molecule in both models. Thus, Nb^{5+} doped TiO_2 is out of the visible region. It has been observed that Sb^{5+} contributes greatly to the valence band and acts as a space-retaining (*p*-type) in Sb^{5+} doped models.

As can be seen in Fig. 5, the Ta^{5+} cation has greatly reduced the band gap energy. There are additional energy levels of Ta^{5+} in the band gap. These levels are the *d* orbitals of Ta^{5+}. The fact that the additional energy levels are close to the conduction band indicates that Ta^{5+} will be an electron scavenger in photocatalytic reactions. Ta^{5+} cation increased the photocatalytic activity of TiO_2 by 503 nm for Model A and 651 nm for Model B.

As can be seen, the V^{5+} cation contributed to the conduction band of TiO_2, causing the band gap to narrow. It shows that doping with V^{5+} shifts the light absorption of TiO_2 the out of the visible region. There are additional energy levels of the d orbitals of V^{5+} in the band gap. Since the additional energy levels are close to the conduction band, V^{5+} acts as an electron scavenger in photocatalytic reactions.

UV-Vis Spectra

UV-vis absorption spectra of the doped and undoped clusters with the lowest energy were calculated by the TD-DFT method. By determining the lowest energy unoccupied orbitals, wavelengths and intensities of possible electronic transitions are obtained. As a result of the calculations, using the wavelengths and intensity values of the electronic transitions obtained UV-vis spectra graphics were drawn with the Gaussian curve fitting technique.

The UV-vis spectra of the clusters obtained by undoping and doping Models A and B are given in Figs. 6, 7 and 8. In these spectra, the wavelength of the first peak is shown by λ1, the second peak λ2, and the third peak λ3. But in some cation-doped models, there is only one peak as seen from the UV-vis absorbance graphics, especially in model B. Maximum wavelength values of Model A and B are given in Table 2.

Model A

The UV-vis absorption wavelength of the undoped model of Model A is 425 nm (Fig. 6). This value corresponds to an electron transition from the valence band to the conduction band of anatase. When the *d* orbitals of the doping cations pass the band gap, they are divided into two parts, one is a low energy t_{2g} (d_{xy}, d_{xz}, d_{yz}) level and the other is the high energy e_g ($d_{x^2-y^2}$, d_{z^2}) level. The e_g level of the d orbitals of titanium is in the upper levels of the conduction band, and the t_{2g} level is in the lower levels of the conduction band. Other peaks in the spectrum belong to the electronic transitions between the valence and conduction bands

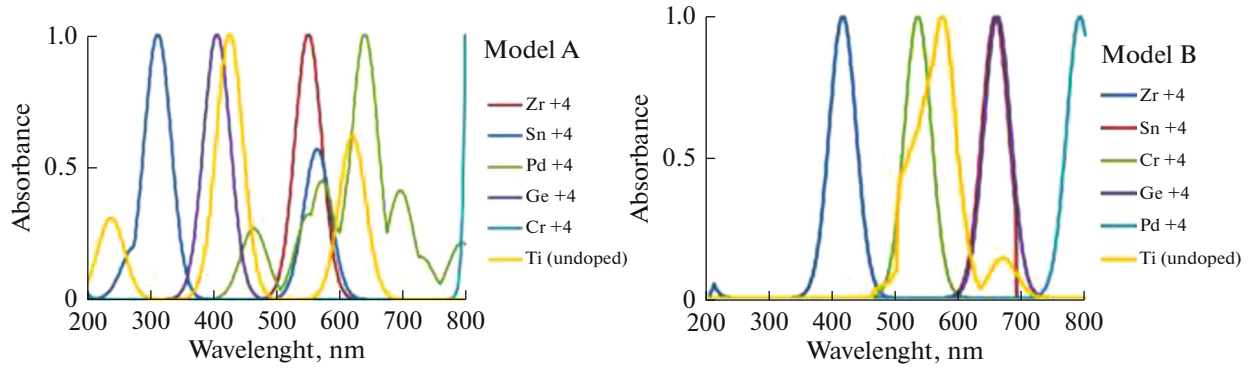

Fig. 7. Calculated UV-vis spectra of doped +4 cations.

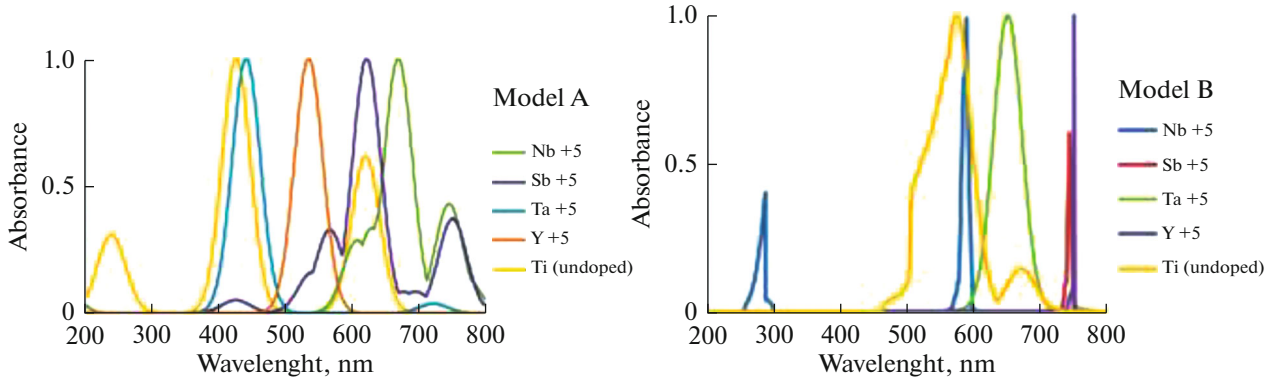

Fig. 8. Calculated UV-vis spectra of doped +5 cations.

of electrons and the e_g and t_{2g} levels in the band gap of the doping metal ion.

The absorption wavelengths of the doped models were given in Table 2. The first absorption wavelengths of the clusters obtained after doping with +3 valent Ru, Os, Co cations were calculated as 474, 480, and 519 nm, respectively. For model A with Ru^{3+} additives, λ1 is approximately the same as for the pure model. On the other hand, λ2 is consistent with the wavelength value corresponding to the electronic transition of the t_{2g} levels of Ru^{3+}. Thus, when model A is doped with +3 value metal cations, the wavelength is shifted towards the visible region.

In the UV-vis spectra of the +4 valence metal ion doped clusters of Model A, the absorbance values of the Zr, Sn, Pd, Cr, and Ge doped models are 545, 558, 793, 799, and 407 nm, respectively as seen in Fig. 7. Thus, as a result of doping with +4 valence ions, the wavelength of these structures shifted to the visible region compared to the pure structure. When these calculated average wavelengths are compared with the wavelength values corresponding to the electronic energy levels as seen in Table 1, it is seen that they are compatible with each other.

The absorbance values of the Nb, Sb, Ta, and V doped models are 739, 745, 435, and 530nm, respectively, for the +5 valent metal cation doped models (Fig. 8). The absorbance wavelengths of the models doped with +5 valence metal ions are also shifted to the visible region. These wavelength values in the UV-vis spectrum show that the electronic transitions are between the valence band and the additional energy levels, and they pass to the conduction band from these levels.

Model B

The maximum wavelength of the UV-vis absorbance spectrum of the undoped Model B is 576 nm. For the +3 valence metal ion doped models, the wavelengths for Ru, Os, and Co are 643, 420, and 371 nm, respectively. Thus, we can say that doping with Ru^{3+} doped ions shifts the absorption wavelength of the model to the visible region. However, the UV-vis absorbance wavelength of the Co^{3+} doped model is lower than the undoped model. The UV-vis absorbance wavelengths of the +3 doped models and the wavelengths corresponding to the transition energy levels (Table1) are compatible with each other.

Table 2. UV-vis absorbance wavelengths of doped Models calculated by DFT method

Metal	λ_1	λ_2	λ_3	λ_1	λ_2	λ_3
	Model A			Model B		
Ru^{3+}	342	474	800	384	643	–
Os^{3+}	384	480	785	420	–	–
Co^{3+}	519	–	–	371	509	602
Zr^{4+}	545	–	–	414		
Sn^{4+}	306	558	–	658	–	–
Pd^{4+}	461	635	793	793	–	–
Cr^{4+}	–	–	799	534	–	–
Ge^{4+}	407	–	–	663	–	–
Nb^{5+}	664	739	–	286	582	–
Sb^{5+}	617	745	–	743	–	–
Ta^{5+}	435	–	–	651	–	–
V^{5+}	530	–	–	750	–	–

The UV-vis spectra of the +4 valent metal ion doped models of Model B are given in Fig. 7. The wavelengths for Zr, Sn, Pd, Cr, and Ge are 414, 658, 793, 534, and 663 nm respectively. As can be seen from the values, wavelengths increased when Model B was doped with the +4 cation, except for the Zr^{4+}. According to these wavelengths, when Model B is doped with +4 valence metal ions, the absorbance values increase as the wavelength shifts toward the visible region.

As seen from the UV-vis spectra of the +5 valent metal ion doped models of Model B in Fig. 8, the wavelengths for Nb, Sb, Ta, and V are 582, 743, 651, and 750 nm, respectively. As with the +5 valence metal ions, the absorption wavelength increased and shifted towards the visible area as a result of the doping, just like the +4 valent metal doping.

The most striking results in the doping of Model B are in the models with +5 valence ion doping. The wavelengths corresponding to the energy values of the model caused the band gap to narrow with the effect of the doped metal ions and thus the wavelength values to increase. The reason why the values in the UV-vis graphs differ from the wavelength values corresponding to the band gap energies is that the transitions are between the conduction and valence bands and the additional energy levels. Frontier molecular orbitals of all molecules studied are given in Fig. SI-4- Fig SI-9.

CONCLUSIONS

In this study, the effect of tri-, tetra-, and penta-metal cations on the electronic structure of TiO_2 was investigated by quantum chemical methods. With some exceptions, doping of TiO_2 with metal cations increased the wavelengths of the clusters by reducing their energy. Zr^{4+} does not contribute to photocatalytic activity in models. Metal cations were found to induce visible light absorption of TiO_2 and affect its photoreactivity. Compared to Model A, doping cation ions tend to stay in the middle of the structure in Model B. When the electronic structures are examined, some of the +3 valence metals contributed to the conduction band and some to the valence band. However, +4 and +5 valence metals contributed to the conduction band (except for Zr^{4+}, Cr^{4+}, and Sb^{5+}). It can be concluded that the doping with +3, +4 and +5 valence cations increase the photocatalytic activity for clusters. According to the calculated UV-vis absorbance results, doping with metal cations extended the wavelengths of TiO_2 clusters compared to undoped TiO_2.

SUPPLEMENTARY INFORMATION

The online version contains supplementary material available at https://doi.org/10.1134/S0018143924700498.

The supporting information includes Electronic energy levels of Model B with +3, +4 and +5 charges metal ion doped and frontier molecular orbitals of the +3, +4 and +5 metals cation doped Model A and Model B.

Fig. SI-1. Electronic energy levels of Model B with +3 metal ion doped.

Fig. SI-2. Electronic energy levels of Model B with +4 metal ion doped.

Fig. SI-3. Electronic energy levels of Model B with +5 metal ion doped.

Fig. SI-4. Frontier molecular orbitals of the +3 metal cation doped Model A.

Fig. SI-5. Frontier molecular orbitals of the +4 metal cation doped Model A.

Fig. SI-6. Frontier molecular orbitals of the +4 metal cation doped Model A.

Fig. SI-7. Frontier molecular orbitals of the +3 metal cation doped Model B.

Fig. SI-8. Frontier molecular orbitals of the +4 metal cation doped Model B.

Fig. SI-9. Frontier molecular orbitals of the +5 metal cation doped Model B.

ACKNOWLEDGMENTS

The authors wish to commemorate this study to beloved professor Zekiye Cinar.

FUNDING

The computing resources of the High-Performance and Grid Computing Center at NCSU were used for DFT calculations. (http://www.ncsu.edu/itd/hpc/main.php).

CONFLICT OF INTEREST

The authors of this work declare that they have no conflicts of interest.

REFERENCES

1. Choa, M.T. and Mohammed, A.R., *J. Alloys Compd.*, 2011, vol. 509, p. 1648. https://doi.org/10.1016/j.jallcom.2010.10.181
2. Shokri, A. and Fard, M.S., *Chem. Pap.*, 2022, vol. 76, p. 5309. https://doi.org/10.1007/s11696-022-02256-3
3. Sood, S., Umar, A., Mehta, S.K., and Kansal, S.K., *J. Colloid Interface Sci.*, 2015, vol. 450, p. 213. https://doi.org/10.1016/j.jcis.2015.03.018
4. Moradi, H., Eshaghi, A., Hosseini, S.R., and Ghani, K., *Ultrason. Sonochem.,* 2016, vol. 32, p. 314. https://doi.org/10.1016/j.ultsonch.2016.03.025
5. Wang, B., Cui, G.Y., Zhang, B.B., Li, Z., Ma, H.X., Wang, W., Zhang, F.Y., and Ma, X.X., *Opt. Mater.,* 2020, vol. 109, p. 110202. https://doi.org/1010.1016/j.optmat.2020.110202
6. Fujishima, F.H., and Honda, K., *Nature*, 1972, vol. 238, p. 37.
7. Nakata, K., and Fujishima, A., *J. Photochem. Photobiol., C,* 2012, vol. 13, p. 169. https://doi.org/10.1016/j.jphotochemrev.2012.06.001
8. Frank, S.N., and Bard, A.J*., J. Am. Chem. Soc.,* 1977, vol. 99, p. 303.
9. Ollis, D.F. and Al-Ekabi, H., *Photocatalytic Purification and Treatment of Water and Air*, Amsterdam: Elsevier, 1993.
10. Matthews, R.W., *J. Catal.,* 1986, vol. 97, p. 565.
11. Matthews, R.W., *J. Catal.,* 1988, vol. 111, p. 264.
12. Tanguay, J.F., Suib, S.L., and Coughlin, R.W., *J. Catal.,* 1989, vol. 117, p. 335.
13. Taraba, K., Haraba, K., and Murata, S., *Sol. Energy*, 1986, vol. 36, p. 159. https://doi.org/10.1016/0038-092X(86)90121-0
14. Albornoz, L.L., da Silva, S.W., Bortolozzi, J.P., Banús, E.D., Brussino, P., Ulla, M.A., and Bernardes, A.M., *Chemosphere*, 2021, vol. 268, p. 128858. https://doi.org/10.1016/j.chemosphere.2020.128858
15. Gurkan, Y.Y., Kasapbasi, E., and Cinar, Z., *Chem. Eng. J.,* 2013 vol. 214, p. 34. https://doi.org/10.1016/j.cej.2012.10.025
16. Turkten, N., and Cinar, Z., *Catal. Today,* 2017, vol. 287, p. 169. https://doi.org/10.1016/j.cattod.2017.01.019
17. Gurkan, Y.Y., Kasapbasi, E., Turkten, N., and Cinar, Z., *Molecules*, 2017, vol. 22, p. 414. https://doi.org/10.3390/molecules22030414
18. Cinar, Z., *Molecules,* 2017, vol. 22, p. 556. https://doi.org/10.3390/molecules22040556
19. Gao, P., Yang, L., Xiao, S., Wang, L. Guo, W., and Lu, J., *Materials*, 2019, vol. 12, p. 814. https://doi.org/10.3390/ma12050814
20. Xavier, A.M., Jacob, I.D., Surender, S., Kumaar, M.S.S., and Elangovan, P., *Inorg. Chem. Commun.,* 2022, vol. 146, p. 110168. https://doi.org/10.1016/j.inoche.2022.110168
21. Ho, W. and Yu, J.C., *J. Mol. Catal. A: Chem.,* 2006, vol. 247, p. 268. https://doi.org/10.1016/j.molcata.2005.11.057
22. In, S., Orlov, A., Berg, R., García, F., Pedrosa-Jimenez, S., Tikhov, M.S., Wright, D.S., and Lambert, R.M., *J. Am. Chem. Soc.,* 2007, vol. 129, p.13790. https://doi.org/10.1021/ja0749237
23. Rao, Z., Lu, G., Mahmood, A., Shi, G., Xie, X., and Sun, J., *Appl. Catal., B.*, 2021, vol. 284, p. 119813. https://doi.org/10.1016/j.apcatb.2020.119813
24. Cheng, R., Xia, J., Wen, J., Xu, P., and Zheng, X., *Nanomaterials,* 2022, vol. 12, p. 1335. https://doi.org/10.3390/nano12081335
25. Ikram, M., Rashid, M., Haider, A., Naz, S., Haider, J., Raza, A., Ansar, M.T., Uddin, M.K., Ali, N.M., Ahmed, S.S., Imran, M., Dilpazir, S., Khan, Q., and Maqbool, M., *Sustain. Mater. Technol.,* 2021, vol. 30, p. e00343. https://doi.org/10.1016/j.susmat.2021.e00343
26. Nur, A.S.M., Sultana, M., Mondal, A., Islam, S., Robel, F. N., Islam, A., and Mst. Sumi, S.A., *J. Water Process. Eng.,* 2022, vol. 47, p. 102728. https://doi.org/10.1016/j.jwpe.2022.102728
27. Li, Z., Shen, W., He, W., and Zu, X., *J. Hazard. Mater.,* 2008, vol. 155, p. 590. https://doi.org/10.1016/j.jhazmat.2007.11.095
28. Karakitsou, K. E., and Verykios, X. E., *J. Phys. Chem.,* 1993, vol. 97, p. 1184. https://doi.org/10.1021/j100108a014
29. Seabra, M.P., Miranda Salvado, I.M., and Labrincha, J.A., *Ceram. Int.,* 2011, vol. 37, p. 3317. https://doi.org/10.1016/j.ceramint.2011.04.127
30. Xu, S.C., Pan, S.S., Xua, Y., Luo, Y.Y., Zhang, Y.X., and Li, G.H., *J. Hazard. Mater.,* 2015, vol. 283, p. 7. https://doi.org/10.1016/j.jhazmat.2014.08.071
31. Herrmann, M., Disdier, J., and Pichat, P., *Chem. Phys. Lett.,* 1984, vol. 108, p. 618. https://doi.org/10.1016/0009-2614(84)85067-8
32. Iwasaki, M., Hara, M., Kawada, H., Tada, H., and Ito, S., *J. Colloid Interface Sci.,* 2000, vol. 224, p. 202. https://doi.org/10.1006/jcis.1999.6694
33. Piatkowska, A., Janus, M., Szymanski, K., and Mozia, S., *Catalysts*, 2021, vol. 11, p. 144. https://doi.org/10.3390/catal11010144
34. Shi, J.W., Zheng, J.T., Hu, Y., and Zhao, Y.C., *Mater. Chem. Phys.,* 2007, vol. 106, p. 247. https://doi.org/10.1016/j.matchemphys.2007.05.042
35. Nyamukamba, P., Tichagwa, L., Mamphweli, S., and Petrik. L., *Int. J. Photoenergy*, 2017, vol. 2017, p. 3079276. https://doi.org/10.1155/2017/3079276

36. Frisch, M.J., Trucks, G.W., Schlegel, H.B., Scuseria, G.E., Robb, M.A., Cheeseman, J.R., Scalmani, G., Barone, V., Petersson, G.A., Nakatsuji, H., Li, X., Caricato, M., Marenich, A.V., Bloino, J., Janesko, B.G., Gomperts, R., Mennucci, B., Hratchian, H.P., Ortiz, J.V., Izmaylov, A.F., Sonnenberg, J.L., Williams-Young, D., Ding, F., Lipparini, F., Egidi, F., Goings, J., Peng, B., Petrone, A., Henderson, T., Ranasinghe, D., Zakrzewski, V.G., Gao, J., Rega, N., Zheng, G., Liang, W., Hada, M., Ehara, M., Toyota, K., Fukuda, R., Hasegawa, J., Ishida, M., Nakajima, T., Honda, Y., Kitao, O., Nakai, H., Vreven, T., Throssell, K., Montgomery, J.A., Jr., Peralta, J.E., Ogliaro, F., Bearpark, M.J., Heyd, J.J., Brothers, E.N., Kudin, K.N., Staroverov, V.N., Keith, T.A., Kobayashi, R., Normand, J., Raghavachari, K., Rendell, A.P., Burant, J.C., Iyengar, S.S., Tomasi, J., Cossi, M., Millam, J.M., Klene, M., Adamo, C., Cammi, R., Ochterski, J.W., Martin, R.L., Morokuma, K., Farkas, O., Foresman, J.B., and Fox, D.J., *Gaussian 16, Revision C.01*, Wallingford, CT: Gaussian, Inc., 2016.
37. Becke. A. D., *J. Chem. Phys.* 1993, vol. 98, p. 5648. https://doi.org/10.1063/1.464913
38. Hehre, W.J., Ditchfield, R., Pople. J.A., *J. Chem. Phys.,* 1972, vol. 56, p. 2257.
39. Kakil, S.A., Abdullah, H.Y., and Abdullah, T.G., *Opt. Quant. Electron.,* 2022, vol. 54, p. 635. https://doi.org/10.1007/s11082-022-03994-0
40. Zhang, X., Liu, Y., Ma, X., Jin, F., Abulimiti, B., and Xiang, M., *Optik,* 2020, vol. 221, p. 165395. https://doi.org/10.1016/j.ijleo.2020.165395
41. Homann, T., Bredow, T., and Jug, K., *Surf. Sci.,* 2004, vol. 555, p. 135. https://doi.org/10.1016/j.susc.2003.12.039